Temperature, Relative Humidity, and Divergence Response to High Rainfall Events in the Tropics: Observations and Models

Toni Mitovski and Ian Folkins

Department of Physics and Atmospheric Science, Dalhousie University, Halifax, Nova Scotia, Canada

Knut von Salzen

Canadian Centre for Climate Modelling and Analysis, University of Victoria, Victoria, British Columbia, Canada

Michael Sigmond

Department of Physics, University of Toronto, Toronto, Ontario, Canada

(Manuscript received 17 September 2009, in final form 18 February 2010)

ABSTRACT

Radiosonde measurements and Tropical Rainfall Measuring Mission (TRMM) 3B42 rainfall are used to construct composite anomaly patterns of temperature, relative humidity, and divergence about high rainfall events in the western Pacific. The observed anomaly patterns are compared with anomaly patterns from four general circulation models [Third and Fourth Generation Atmospheric General Circulation Model (AGCM3 and AGCM4), Geophysical Fluid Dynamics Laboratory Climate Model version 2.1 (GFDL CM2.1), and European Center Hamburg Model version 5 (ECHAM5)] and two reanalysis products [40-yr ECMWF Re-Analysis (ERA-40) and ERA-Interim]. In general, the models and reanalyses do not fully represent the timing, strength, or altitude of the midlevel congestus divergence that precedes peak rainfall or the midlevel stratiform convergence that occurs after peak rainfall. The surface cold pools that develop in response to high rainfall events are also either not present or somewhat weaker than observations. Surface cold pools originate from the downward transport within mesoscale downdrafts of midtropospheric air with low moist static energy into the boundary layer. Differences between the modeled and observed response to high rainfall events suggest that the convective parameterizations used by the models and reanalyses discussed here may under-represent the strength of the mesoscale downdraft circulation.

1. Introduction

The convective parameterizations of climate models are typically adjusted to give reasonable climatological distributions of temperature, water vapor, convective mass transport, and rainfall in the tropics. However, these climatological distributions arise from the cumulative impact of individual moist convective events that occur on much shorter time scales. Realistic convective parameterizations should be able to simulate the short-time-scale interactions between moist convection and the background atmosphere.

Observations from field campaigns and satellites over the past 40 years, as well as simulations from cloud resolving models, have shown that tropical convective clouds often organize themselves in a characteristic manner that has recently been dubbed the "building block" pattern (Mapes et al. 2006). Congestus clouds often precede deep convection and give rise to a midlevel divergence prior to deep convective rainfall (Thompson et al. 1979; Mapes and Lin 2005; Mapes et al. 2006). Cumulus congestus development is aided and partially controlled by a midlevel cooling that both precedes and follows maximum rainfall (Sherwood and Wahrlich 1999; Mapes et al. 2006; DeMott et al. 2007; Mapes et al. 2009). Midlevel moistening from cumulus congestus clouds appears to promote the subsequent development of deep convection (Johnson et al. 1999; Sherwood 1999; Sobel et al. 2004; DeMott et al. 2007).

Corresponding author address: Toni Mitovski, Department of Physics and Atmospheric Science, Dalhousie University, Halifax, NS B3H 3J5, Canada.
E-mail: tn648214@yahoo.com

Deep convective clouds inject large amounts of condensate into the upper troposphere. This condensate contributes to the development of precipitating stratiform anvil clouds that can persist for several hours or more following deep convection. It has been estimated that 40% of tropical rainfall originates from stratiform clouds (Schumacher and Houze 2003). The base of precipitating stratiform anvil clouds is usually near the 0°C melting level, or about 5 km (Zipser 1977). When stratiform precipitation falls through unsaturated air below the melting level, it can generate negatively buoyant mesoscale downdrafts that penetrate to the surface (Zipser 1969, 1977; Barnes and Garstang 1982). Precipitating stratiform anvil clouds are typically convergent at midlevels (Reed and Recker 1971; Mapes and Houze 1995; Mapes and Lin 2005). This convergence is probably at least partially attributable to a rapid increase in downdraft mass flux near the melting level (Johnson 1976; Folkins 2009).

By mass continuity, the downdrafts associated with stratiform precipitation must induce compensatory uplift in their environment. On shorter spatial scales, this uplift is mediated by density currents and pressure gradient accelerations that can generate squall lines (Tepper 1950). On larger spatial scales, this uplift is generated by waves. The cooling and moistening of the background atmosphere associated with this wave-induced compensatory uplift can also trigger further downstream convection (Mapes 1993; Mapes and Houze 1995; Fovell et al. 2006).

Many of the previous studies examining the short-time-scale interactions between tropical convection and the background atmosphere have generated composite analyses using output from cloud resolving models, data from field programs of several months in duration, 40-yr European Centre for Medium-Range Weather Forecasts (ECMWF) Re-Analysis (ERA-40) (Benedict and Randall 2007), or National Centers for Environmental Prediction–National Center for Atmospheric Research (NCEP–NCAR) reanalysis (Maloney and Hartmann 1998). Here, we develop composite anomaly patterns from 11 years of radiosonde data (1998–2008) at 10 locations in the western tropical Pacific. High rainfall events at these radiosonde locations were identified using the 3-h gridded rainfall product 3B42 from the Tropical Rainfall Measuring Mission (TRMM) (Kummerow et al. 1998). The radiosonde measurements were used to construct temperature, relative humidity, and mass divergence anomaly patterns about TRMM high rainfall events. These anomaly patterns extend from 24 h prior to peak rainfall to 24 h after peak rainfall.

In the building block model, the interactions between the three basic cloud building blocks—cumulus congestus, deep, and stratiform—promote the organization of tropical moist convection into coherent propagating systems
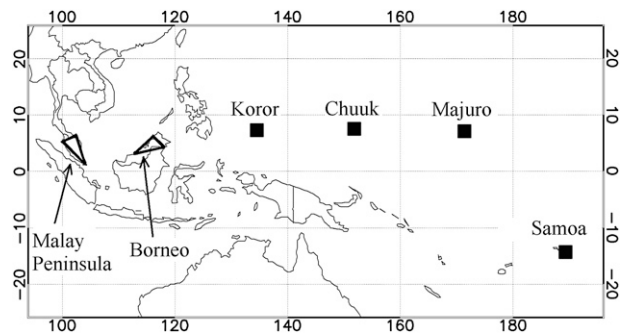

FIG. 1. Solid squares indicate the locations of the radiosonde stations used to calculate temperature and relative humidity anomaly patterns at remote marine locations. The two triangular radiosonde arrays were used mainly to calculate mass divergence patterns about high rainfall events. The array on the Malay Peninsula consisted of stations Singapore (Changi), Kota Bharu, and Penang (Bayan Lepas). The array on the island of Borneo consisted of Tawau, Bintulu, and Kota Kinabalu.

across a wide range of spatiotemporal scales. Parameterizations of tropical convection that exhibit these types of interactions should be better able to reproduce the observed spatial and temporal variability of deep convection. We therefore examine the interaction of high rainfall events with the background atmosphere in four climate models, and in two reanalysis datasets.

The paper is divided into five sections. In section 2, we discuss the radiosonde dataset, the TRMM 3B42 gridded rainfall product, the general circulation models, and the reanalysis products used in the study. In section 3, we discuss the methods used to construct the observed anomaly patterns. These patterns are discussed in section 4. In section 5, we discuss the construction of anomaly patterns in the models and compare the anomaly patterns from the models with observations. Section 6 is a summary of our results.

2. Datasets

a. IGRA

The Integrated Global Radiosonde Archive (IGRA) is produced by the National Climatic Data Center (NCDC). This radiosonde archive is derived from 11 different sources, and contains records from more than 1500 stations (Durre et al. 2006). Most of the stations have twice daily records for the past 20 years. We used temperature, relative humidity, and wind data for 11 years (1998–2008) on standard pressure levels (1000, 925, 850, 700, 500, 400, 300, 250, 200, 150, 100 hPa). The locations of the radiosonde stations used in this study are shown in Fig. 1. The stations at Koror, Chuuk, Majuro, and Samoa were used to construct temperature and relative humidity anomaly patterns that should be representative of the western tropical Pacific Ocean. Figure 1 also shows a triangular

radiosonde array on the island of Borneo and another on the Malay Peninsula. These arrays were used to construct divergence anomaly patterns about high rainfall events. The wind measurements from these triangles can be expected to be strongly influenced by the diurnal cycle in moist convection over land and by local sea breeze circulations.

b. TRMM

The TRMM 3B42 gridded rainfall product has a temporal resolution of 3 h centered at the standard synoptic times (0000, 0300, 0600, 0900, 1200, 1500, 1800, and 2100 UTC), and a spatial resolution of 0.25°. We used data from 1998 to 2008. The TRMM data come from several satelliteborne sensors including a precipitation radar, multichannel microwave radiometer, and visible and infrared sensors (Kummerow et al. 1998). The TRMM 3B42 algorithm uses a combination of high-quality microwave and IR precipitation estimates to derive calibration coefficients and adjust the IR estimates from other satellite observations. The high-quality estimates are used where available. The remaining grid boxes are filled with the adjusted IR estimates (Huffman et al. 2007). The TRMM 3B42 rainfall estimates are then scaled to match monthly measurements from rain gauges.

c. AGCM3

The Third Generation Atmospheric General Circulation Model (AGCM3) is maintained by the Canadian Centre for Climate Modeling and Analysis (CCCma). The model output is archived on a $2.8° \times 2.8°$ grid every 3 h. The results in this paper are based on 10 years of AGCM3 output. Deep convection is parameterized using the Zhang and McFarlane (ZM) mass flux scheme (Zhang and McFarlane 1995; McFarlane et al. 2005). The ZM scheme represents deep convection using plumes with various entrainment rates. In AGCM3, as well as in the other models discussed here, the temperature, humidity, and wind (or divergence) fields refer to model variables at one time step, while precipitation is accumulated over a 3-h period (or for some models, a 6-h period).

d. AGCM4

AGCM4 is a revised version of AGCM3. The output was stored at a spatial resolution of $2.8° \times 2.8°$ every 6 h. AGCM4 has a new radiation code, prognostic cloud microphysics, and a shallow cumulus scheme (von Salzen et al. 2005). It continues to use the ZM scheme for deep convection. This study uses 5 years of AGCM4 output.

e. GFDL CM2.1

The Geophysical Fluid Dynamics Laboratory Climate Model version 2.1 (GFDL CM2.1) is a coupled ocean–

atmosphere model. The output was stored at a resolution of $2.0°$ latitude $\times 2.5°$ longitude, every 6 h. The model uses the Relaxed Arakawa–Schubert (RAS) parameterization for deep convection (Delworth et al. 2006). This study used 5 years of data (1996–2000) from a twentieth-century climate run.

f. ECHAM5

The output from the European Center Hamburg Model Version 5 (ECHAM5) (Roeckner et al. 2003) was stored at a resolution of $1.9° \times 1.9°$, every 6 h. ECHAM5 employs a mass flux scheme for shallow, midlevel, and deep convection (Tiedtke 1989), with modifications for penetrative convection (Nordeng 1994). The stratiform scheme consists of prognostic equations representing liquid water and ice, a cloud microphysical scheme (Lohmann and Roeckner 1996), and a statistical cloud cover scheme (Tompkins 2002). We used 5 years of data (2001–06) from a 2001–50 scenario run.

g. ERA-40 and ERA-Interim

In addition to output from four general circulation models, we also examined the ERA-40 and ERA-Interim reanalysis products from ECMWF (Uppala et al. 2005). ERA-40 output is archived at a resolution of $2.5° \times 2.5°$, every 6 h. ERA-Interim output has a slightly finer spatial resolution of $1.5° \times 1.5°$ but is also stored every 6 h. We used 5 years of data from both ERA-40 (1997–2001) and ERA-Interim (2003–07). The instantaneous temperature, relative humidity, and wind fields are stored at the standard synoptic times of 0000, 0600, 1200, and 1800 UTC. A cumulative precipitation forecast is issued at 0000 UTC for the 0000–0600 UTC 6-h time interval. This was used to obtain an average rain rate at 0300 UTC. A second precipitation forecast is issued at 0000 UTC for the 0000–1200 UTC 12-h time interval. This was used to obtain a forecast average rain rate at 0900 UTC (after first subtracting the first 0000–0600 UTC cumulative precipitation forecast). Cumulative 6-h rain rate forecasts centered at 1500 and 2100 UTC, based on precipitation forecasts at 1200 UTC, were obtained in a similar manner.

3. Procedure for calculating observed anomaly patterns

a. Temperature anomaly patterns

Composite temperature anomaly patterns about high rainfall events were constructed for the four remote island radiosonde stations indicated in Fig. 1 by solid squares. TRMM 3B42 rainfall was first averaged over a $2° \times 2°$ region centered at each island. This was done to facilitate comparisons with the anomaly patterns of the
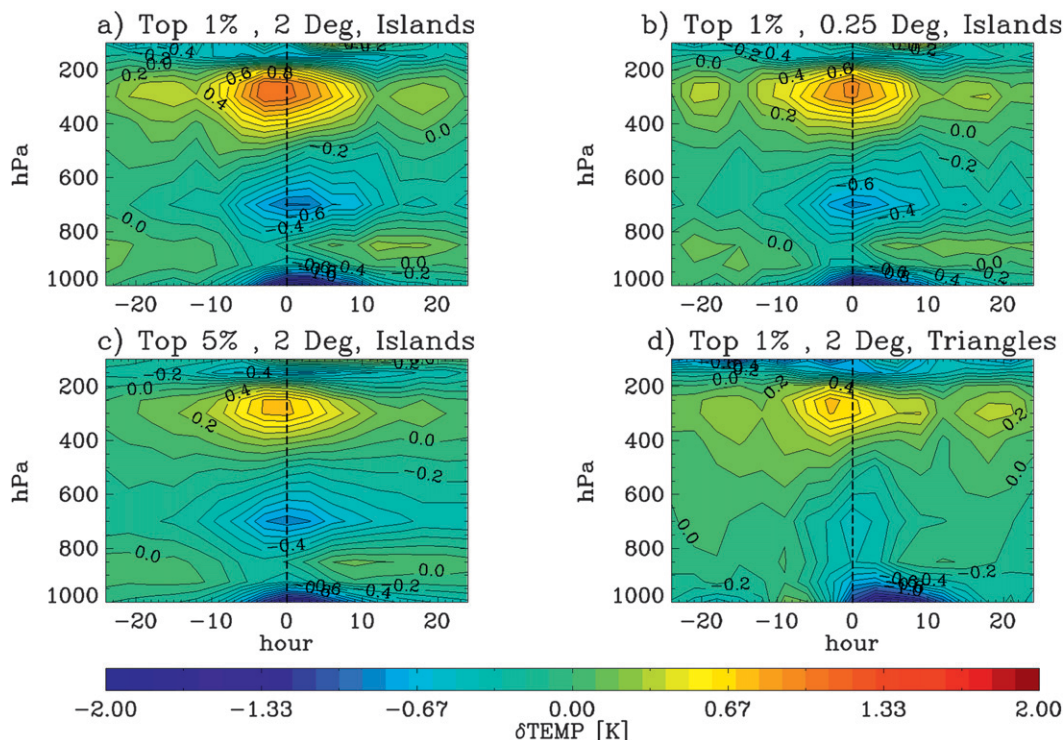
FIG. 2. Time–height plots of the observed temperature anomaly pattern about high rainfall events ($t = 0$ on the horizontal axis). Values at negative lags refer to temperature anomalies prior to peak rainfall. Values at positive lags refer to temperature anomalies after peak rainfall. The anomalies were calculated using radiosonde temperature soundings and 3-h TRMM 3B42 rainfall. (a)–(c) Anomaly patterns averaged over the four remote radiosonde locations shown in Fig. 1, but with differing rain event thresholds and averaging regions: (a) the top 1% of $2° \times 2°$ rain events (centered at the radiosonde locations), (b) the top 1% of $0.25° \times 0.25°$ rain events, and (c) the top 5% of $2° \times 2°$ rain events. (d) The temperature anomalies calculated using the soundings from the six land stations (vertices of the triangles shown in Fig. 1).

models. High rainfall events were defined as events at which the 3-h TRMM rainfall rate within each $2° \times 2°$ region centered at a radiosonde location was in the highest 1% for that month, averaged over the 11 years of the TRMM record. After determining the times of these high rainfall events, we searched for radiosonde profiles, at each location, that had occurred 24 h before, or 24 h after, one of these events. A time difference was assigned to each radiosonde profile based on the difference between the launch time of each radiosonde and the time of the TRMM rainfall event. We then calculated the anomaly of the radiosonde temperature profile with respect to an 11-year climatology. This climatology was constructed from all radiosonde profiles at that location that had occurred during the same month, and also had the same launch time, as the radiosonde profile close to a high rainfall event. This was done to remove the influence of the seasonal and diurnal cycles on the temperature anomalies. The various radiosonde temperature anomaly profiles were then grouped together in 3-h time bins, ranging over the 48-h time interval, and then combined

to create a composite anomaly pattern as a function of pressure and time.

Despite their differing geographic locations, the temperature anomaly patterns of the four remote island stations were quite similar. The four patterns were therefore averaged together to create an overall anomaly pattern. This is shown in Fig. 2a. There were roughly 1300 high rainfall events over the 11-yr period from all four locations. Within the 48-h time window about these 1300 events, there were approximately 4000 temperature available soundings.

One would expect temperature anomaly patterns about high rainfall events to be sensitive to the intensity threshold used to define the events and to the size of the area over which events are spatially averaged. Figure 2b shows the temperature anomaly pattern generated by retaining the original 0.25° resolution of the TRMM 3B42 dataset, but again using the top 1% events with a $0.25° \times 0.25°$ box. This pattern is very similar to the pattern obtained by degrading the original resolution to 2.0°. Figure 2c shows the temperature anomaly pattern generated using the
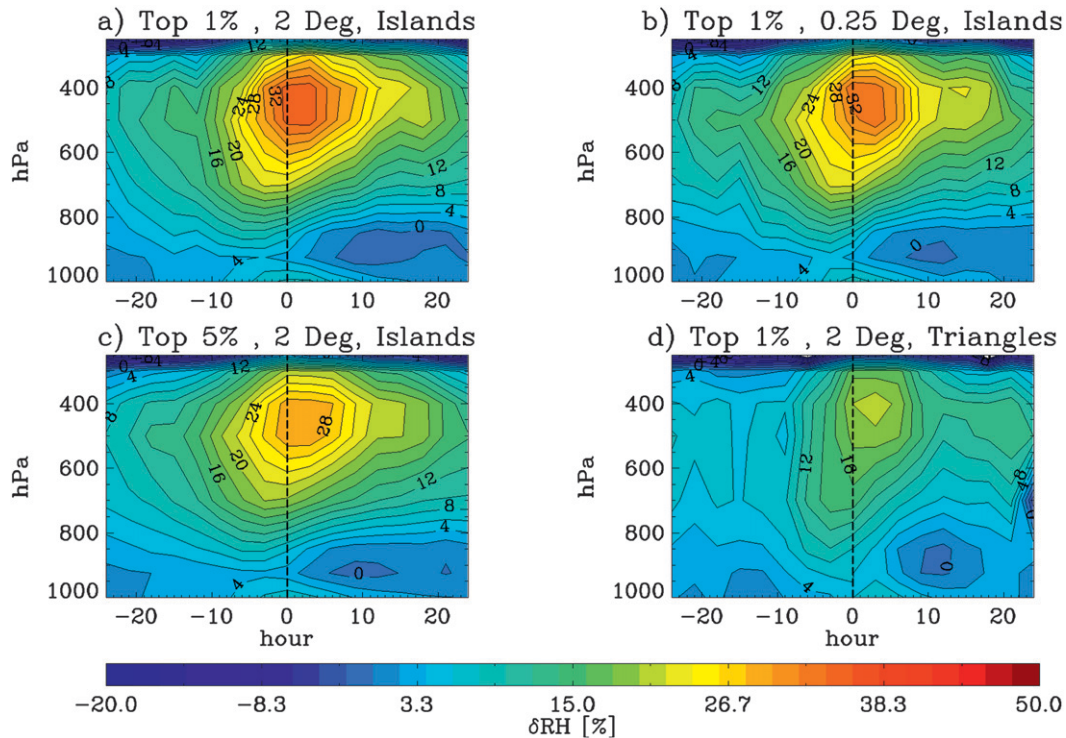
FIG. 3. Time–height plots of observed relative humidity anomaly patterns about high rainfall events ($t = 0$). (a)–(c) Averages using data from the four remote tropical islands shown in Fig. 1. (d) Plot is based on radiosonde profiles from the two triangular radiosonde arrays shown in Fig. 1.

highest 5% TRMM 3B42 rainfall events, but again using the 2.0° resolution. The relaxation of the event definition decreases the magnitude of the temperature anomalies by roughly one-third. However, the shape of the overall pattern is similar to the pattern obtained by using the higher rainfall event threshold. The near invariance of the temperature anomaly pattern with respect to changes in event definition, with respect to both spatial size and intensity, supports previous arguments that the building block pattern recurs within organized tropical convection across a broad range of spatiotemporal scales (Mapes et al. 2006).

Moist convection over land differs from moist convection over the ocean. For consistency with the temperature and relative humidity anomaly patterns, and to facilitate comparisons with the models, it would have been desirable to also calculate the divergence anomaly pattern using horizontal wind measurements from remote ocean stations. However, a sufficiently close set of routine measurements from tropical islands was not available. We instead used the two triangular radiosonde arrays shown in Fig. 1. There is no guarantee that the divergence patterns from these land stations will resemble those over the ocean.

Figure 2d shows the temperature anomaly patterns of the top 1% rainfall events at the arrays, defined using

$2° \times 2°$ boxes centered at the two arrays. The shapes of the temperature anomaly patterns of the two arrays are similar to the anomaly patterns of the remote oceanic islands. However, the temperature response of the two arrays is about 50% weaker than over the islands. This difference probably arises from the smaller spatial scale of the rainfall events over the arrays. For every top 1% $2° \times 2°$ rainfall event over the arrays, the average $6° \times 6°$ rainfall rate centered on the array is 0.28 times the $2° \times 2°$ rainfall rate. For each top 1% $2° \times 2°$ rainfall event over the remote ocean islands, the average $6° \times 6°$ rainfall rate centered on the island is 0.37 times the $2° \times 2°$ rainfall rate.

b. Relative humidity anomaly pattern

Relative humidity anomaly patterns about high rainfall events were constructed using the same procedure used for the temperature anomaly patterns. Figure 3a shows an average relative humidity anomaly pattern for the four remote island radiosonde locations. Radiosonde humidity measurements tend to be less accurate at the cold temperatures of the upper troposphere. Relative humidity anomalies are therefore not shown above 250 hPa. Figure 3b shows a relative humidity anomaly pattern calculated in the same manner as for Fig. 3a, but with the size of the rainfall area decreased from 2° to 0.25°. Figure 3c shows a relative humidity anomaly
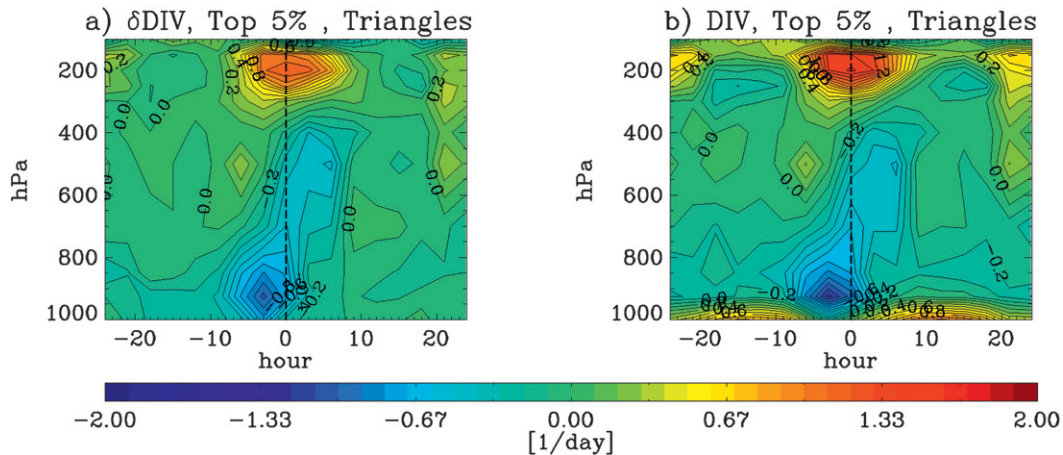
FIG. 4. Time–height plots of the observed anomaly divergence and divergence patterns about high rainfall events ($t = 0$).
(a),(b) Calculated using the top 5% rainfall events averaged over the two radiosonde arrays shown in Fig. 1.

pattern in which the rainfall event intensity threshold is relaxed from 1% to 5%. As with the temperature anomaly pattern, the shape of the relative humidity anomaly pattern is nearly insensitive to changes in rainfall event definition.

Figure 3d shows the relative humidity anomaly of the two arrays is weaker than that over the remote ocean islands. This is also likely due to the shorter spatial scale of the rain events over the two arrays. However, the shape of the relative anomaly patterns of the two arrays is again very similar to the anomaly patterns over the oceanic islands.

In general, changes in relative humidity are due to some combination of changes in temperature and specific humidity. It can be shown, however, that the observed specific humidity anomaly pattern is similar to the observed relative humidity anomaly pattern, so that the relative humidity anomalies shown in Fig. 3 are mainly due to changes in specific humidity.

c. Divergence anomaly pattern

The two radiosonde arrays used here to calculate the divergence patterns are shown in Fig. 1. The area of each array is approximately 65 000 km^2, comparable with the area of a GCM grid box. The calculation of the divergence of an array, at any pressure level, requires simultaneous knowledge of the winds at each of the three radiosonde locations. Because of missing wind measurements from one or more stations, complete divergence profiles were not available at all radiosonde launch times. We therefore defined high rainfall events as those that were in the top 5% of monthly TRMM 3B42 rainfall, averaged over each array. Figure 4 shows the divergence anomaly pattern of the two arrays, as well as the divergence pattern itself. Other than averaging over a different spatial area,

the divergence and divergence anomaly patterns were calculated using a procedure identical to that used for the temperature and relative humidity anomaly patterns.

The dominant error in the calculation of the divergence at any level is probably the error associated with the interpolation of the horizontal winds at any two vertices of an array to the midpoint of the line connecting them. This error is difficult to quantify. However, the high rainfall event divergence patterns of the two arrays are similar, so that the divergence features shown in Fig. 4 are likely to be characteristic of the two arrays.

The statistical representativeness of the divergence patterns is not as high as for the temperature and relative humidity anomaly patterns. The number of divergence measurements for each array within each time bin is 300–350 per level in the lower troposphere, but decreases to 70–80 per level in the upper troposphere.

4. Discussion of observed anomaly patterns

a. Discussion of the observed temperature anomaly pattern

The solid black curve in Fig. 5g shows the variation in TRMM 3B42 rainfall with time, averaged over the roughly 1300 high rainfall events at the four radiosonde locations. Rainfall during high rainfall events (i.e., zero time lag) exceeds 5 mm h^{-1}, corresponding to a roughly 20-fold increase from the climatological rain rate at these locations.

Figure 5a shows that the dominant features in the observed temperature response to high rainfall events are an upper-level warming of roughly 1 K, a 0.8-K midlevel cooling centered at 500 hPa, and a boundary layer cooling below 900 hPa of up to 2 K. All three features are
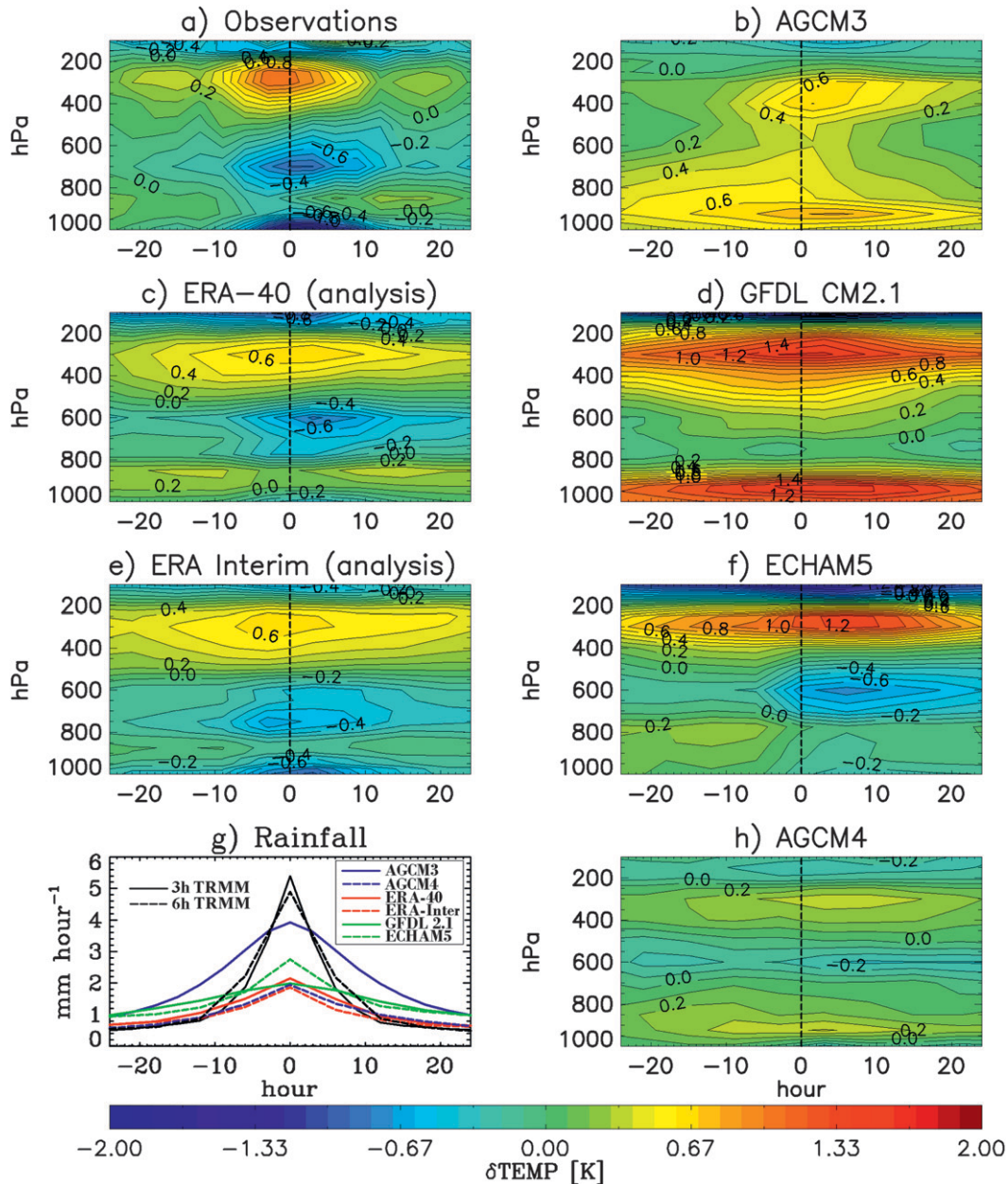
FIG. 5. (a) The observed temperature anomaly pattern is compared with the temperature anomaly pattern calculated from (b) AGCM3; (c) ERA-40; (d) GFDL CM2.1; (e) ERA-Interim; (f) ECHAM5; and (h) AGCM4. (g) Variation in rainfall with time before and after the top 1% rainfall events.

nearly symmetric about zero lag, and extend from roughly 10 h prior to peak rainfall until 10 h after peak rainfall. There is a tendency for the midlevel and boundary layer cooling to be preferentially distributed toward positive lag times. This is particularly true in the case of the boundary layer cooling of the two radiosonde arrays, shown in Fig. 2d.

Temperature soundings taken after the passage of convective squall lines, and under precipitating anvil clouds,

often show a cool near saturated layer of air in the lowest few hundred meters. This layer is separated by an inversion from an overlying layer of warm dry air, between roughly 950 and 850 hPa (Zipser 1977). In Figs. 2 and 3, the warm dry layer that gives rise to these characteristic "onion" shaped soundings occurs between 950 and 800 hPa, and is strongest 10 to 20 h after peak rainfall.

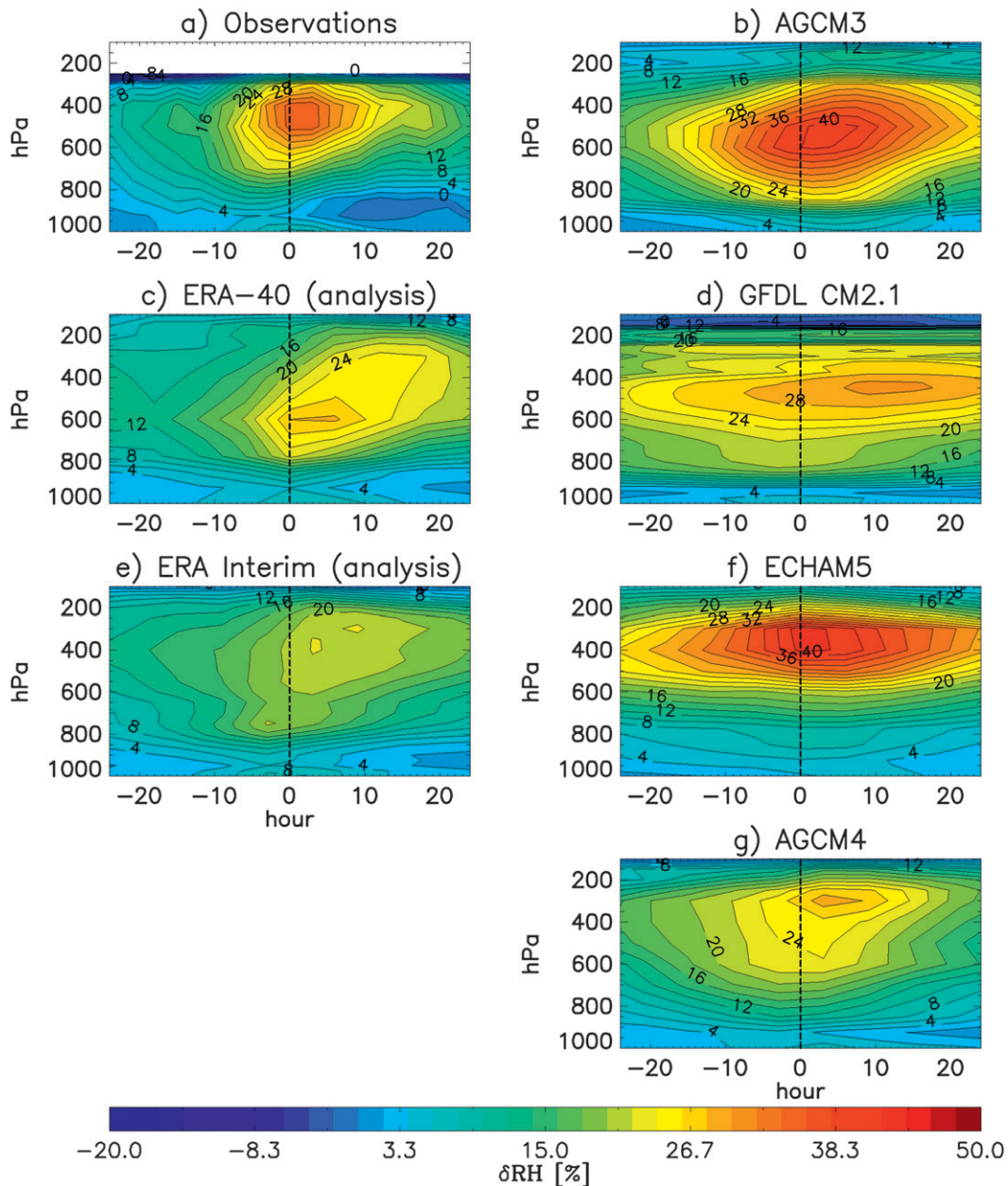Tropical convection produces a long range temperature response in the background atmosphere. The

FIG. 6. (a) The observed relative humidity anomaly pattern is compared with the relative humidity anomaly patterns from (b) AGCM3, (c) ERA-40, (d) GFDL CM2.1, (e) ERA-Interim, (f) ECHAM5, and (g) AGCM4 model output.

lower-tropospheric cooling has a spatial scale of roughly 1000 km, while the upper-tropospheric warming has a spatial scale of 2000 km (Folkins et al. 2008). It is therefore likely that temperature anomalies prior to the rainfall maxima partially reflect the remote impact of the propagation of convective systems toward the radiosonde location, rather than simply the effects of local convection. Similarly, temperature anomalies at positive time lags will also reflect the remote effects of convective systems outside the 2° by 2° averaging region.

b. Discussion of the observed relative humidity anomaly pattern

Figure 6a shows the observed relative humidity anomaly pattern associated with the top 1% high rainfall events at the four island stations. Deep convection gives rise to positive relative humidity anomalies at all altitudes except within the boundary layer. There is a broad upper-level relative humidity maximum centered several hours after peak rainfall. Between 900 and 700 hPa, relative humidity
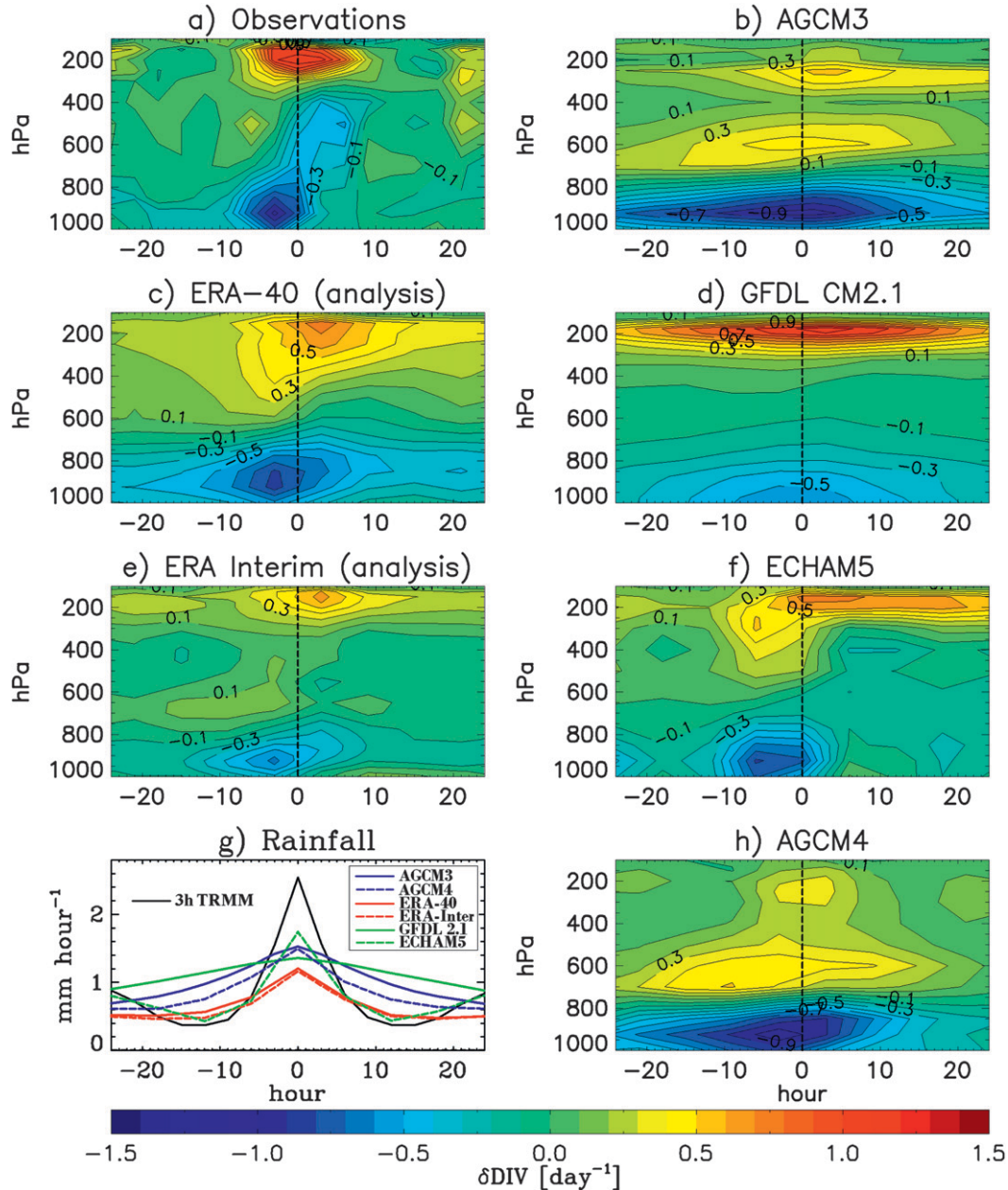
FIG. 7. Time–height plots of the mass divergence anomaly about a maximum precipitation reference time. (a) The observed divergence was calculated from soundings of the horizontal wind at the two triangular arrays shown in Fig. 1, using the top 5% rainfall events within these arrays as determined from TRMM 3B42 rainfall. The remaining divergence patterns are taken from climate models or reanalyses: (b) AGCM3, (c) ERA-40, (d) GFDL CM2.1, (e) ERA-Interim, (f) ECHAM5, and (h) AGCM4. (g) The variation in TRMM 3B42, modeled, and analyses rainfall, averaged over all top 5% events.

peaks approximately 4–5 h prior to peak rainfall. Contours of constant relative humidity then tilt upward to the right for the next 20 h. The slope in midlevel relative humidity prior to deep convection has been previously interpreted as a consequence of the development and growth of congestus clouds prior to deep convection (Takayabu et al. 1996; Mapes et al. 2006).

c. Discussion of the observed divergence anomaly pattern

Figure 7g shows the variation of observed rainfall with time during rainfall events within the two radiosonde arrays on Borneo and the Malay Peninsula. Peak rainfall during these events is roughly 2.5 mm h^{-1}, about half

the intensity of the rainfall events over the tropical islands. This is mainly a reflection of the use of a 5% rather than 1% event threshold. There is also a pronounced diurnal cycle, reflecting the stronger diurnal cycle in tropical deep convection over land.

Figure 7a shows the divergence anomaly pattern associated with high rainfall events. Boundary layer convergence starts to intensify 10 h prior to maximum rainfall. The onset of this low-level convergence is coincident with the emergence of a midlevel divergence feature centered at 500 hPa (Schumacher et al. 2008). The height and timing of this feature suggest that it arises from cumulus congestus outflow. These clouds are probably responsible for the observed midlevel relative humidity maximum prior to peak rainfall.

The vertical growth of congestus clouds is believed to be strongly affected by the stability of the atmosphere. Figure 2 shows that a midlevel cold anomaly develops prior to maximum rainfall. This cold anomaly would increase the atmospheric stability near 500 hPa and contribute to the development of what is known as melting-level inversions (Johnson et al. 1996). The existence of these stability layers favors detrainment from cumulus congestus clouds near 500 hPa (Zuidema 1998; Johnson et al. 1999; Folkins 2009).

Deep convective outflow gives rise to a pronounced maximum in upper-level divergence between 300 and 150 hPa, centered at peak rainfall. The temporal and vertical separation between the congestus and deep outflow divergence maxima suggests that they originate from distinct cloud types with different convective heating profiles. The 500-hPa midlevel convergence maximum, which occurs after peak rainfall, is probably due to some combination of an increase in downdraft mass flux at the melting level and an increase in upward mass flux within stratiform anvils (Houze 2004). The congestus divergence and stratiform convergence are of similar magnitude and occur at similar heights.

5. Modeled anomaly patterns

Rainfall events were identified in the models and reanalyses using the same procedure as described for the TRMM 3B42 rainfall events, except that the native horizontal resolution of the models was retained in each case. The grid cells selected from each model were those nearest the radiosonde locations or arrays. Figure 5g shows the average variation of rainfall with time during the modeled rainfall events over the remote marine radiosonde stations. In all models, the rainfall events are less intense than in TRMM 3B42.

The weakness of the modeled rainfall events is partly due to the longer temporal resolution of the model output.

For all models except AGCM3, the rainfall events have been defined using accumulated rainfall output at 6 h rather than 3 h. For comparison, we also show the variation of rainfall with time if the TRMM rainfall events are defined using a version of the TRMM 3B42 dataset in which the temporal resolution is degraded from 3 to 6 h. The 6-h TRMM rainfall event profile, as represented by the dashed black curve in Fig. 5g, is slightly less intense and less temporally confined than the 3-h TRMM. However, the TRMM 6-h rainfall event profile continues to be more sharply peaked than the models.

In some cases, the weaker rainfall event intensity of the models may also be partly due to the fact that their spatial resolution is slightly larger than the $2° \times 2°$ spatial resolution used to define the TRMM rainfall events. It is well known, however, that global models tend to exhibit less rainfall variance than observations (Scinocca and McFarlane 2004; DeMott et al. 2007). Models produce light precipitation (<10 mm day^{-1}) more often than observed and underestimate strong precipitation (>10 mm day^{-1}) (Sun et al. 2006; Dai 2006).

Despite the differences in rainfall event intensity, the observed invariance of the temperature and relative humidity anomaly patterns with respect to changes in event definition suggests that, in principle, models should be able to reproduce the basic aspects of the building block pattern, despite their reduced rainfall variance.

Figure 5 shows that each of the four general circulation models generates an upper-tropospheric warming associated with high rainfall events, albeit with varying degrees of realism. In general, the upper-tropospheric warming in the models is less temporally confined than in observations.

None of the climate models exhibits the strong boundary layer cooling coincident with maximum rainfall seen in the observations. The GFDL CM2.1 and AGCM3 models show a boundary layer warming. This discrepancy is probably a reflection of the absence, from these models, of downdrafts originating at midlevels capable of injecting air with low moist static energy into the boundary layer (Barnes and Garstang 1982).

Although there is a narrow layer of midlevel cooling in the AGCM4 model, the only climate model showing a pronounced midlevel cooling is ECHAM5. This cooling occurs, however, mostly after peak rainfall. The observed midlevel cooling is almost symmetric about peak rainfall.

As would be expected, the temperature anomaly patterns of the two reanalyses are closer to observations. The greater dispersion of the upper-tropospheric warming in the two reanalyses can probably be attributed to the greater width of the rainfall event maxima in these two models. Despite the input of surface observations, the ERA-40 temperature anomaly pattern does not exhibit

surface cold pools in association with deep convection. There is some boundary layer cooling in ERA-Interim, but it is somewhat weaker than observed. Both reanalyses show a pronounced midlevel cooling. The absence, or weakness, of the surface cold pools in the models and reanalyses is unfortunate. The downdrafts associated with surface cold pools have been associated with the mesoscale organization of tropical convection (Tompkins 2001) and the emergence of the congestus outflow mode (Folkins 2009; Khairoutdinov et al. 2009).

The right-hand panels of Fig. 6 show the change in relative humidity of the four climate models in response to high rainfall events. All four models show extensive upper-level moistening. This moistening tends to be less confined both temporally and in the vertical than the observed moistening. The observed low-level premoistening and tilt occurs to some degree in the AGCM4 climate model, and in the analyses, but is less evident in the other three climate models.

The right-hand panels of Fig. 7 show the divergence anomaly pattern of the four climate models. As would be expected, all models show a strong boundary layer convergence and upper-level divergence in association with high rainfall events. Most models and analyses show at least some suggestion of a distinct congestus outflow mode. In general, however, the timing, strength, and height of the congestus outflow mode are not realistically represented.

ECHAM5 is the only climate model to show a postconvective midlevel stratiform convergence. It is, however, somewhat weaker and higher than the observed convergence. The two reanalyses do not fully represent the observed midlevel congestus divergence–stratiform convergence dipole. ERA-Interim does show a midlevel divergence dipole. But the dipole is weaker than observed, and there is a vertical misalignment between the divergence prior to maximum rainfall and the convergence after maximum rainfall.

As with the temperature and relative humidity anomaly patterns, some of the differences between the observed and modeled divergence patterns are probably a result of differences in rainfall variance. The solid black line in Fig. 7g shows the averaged variation in TRMM 3B42 rainfall with time during the top 5% rainfall events inside the two radiosonde arrays shown in Fig. 1. The other curves show the top 5% rainfall events in the four models and two reanalyses. As was the case with the top 1% rainfall events, the observed rainfall events are more sharply peaked than the models.

6. Summary

We have used radiosonde measurements and TRMM 3B42 rainfall estimates to confirm and extend the building block model of tropical convection. High rainfall rates are coincident with three distinct temperature anomalies: upper-level warming, midlevel cooling, and boundary layer cooling. Congestus clouds moisten the midtroposphere prior to peak rainfall. This contributes to an upward tilt in relative humidity contours as rainfall proceeds. A midlevel congestus divergence–stratiform convergence dipole is symmetrically distributed about peak rainfall. After peak rainfall, a warm dry layer develops near 850 hPa. The temperature and relative humidity anomaly patterns of high rainfall events are insensitive to how high rainfall events are defined, at least in terms of their intensity and spatial extent. This supports previous arguments that the building block conceptual picture of moist convection is applicable across a broad range of spatiotemporal scales (Mapes et al. 2006).

The observed divergence anomaly pattern was generated using two radiosonde arrays over land. There is no guarantee that this divergence pattern will also be representative of the tropical oceans. However, the similarity between the temperature and relative humidity anomaly patterns of the land arrays to those of the remote ocean islands suggests that the divergence patterns should also be similar.

We compared the observed anomaly patterns with those generated by high rainfall events in four climate models and in two reanalysis datasets. Some aspects of the short-time-scale interactions between high rainfall events and the background atmosphere are not fully resolved in models. In particular, the midlevel congestus divergence–stratiform convergence dipole is not well represented in either the models or the reanalyses. The ECHAM5 model and ERA-Interim analysis do successfully exhibit a midlevel divergence dipole. However, the timing, strength, and altitude of these dipoles are not fully consistent with observations.

Most of the models and reanalyses do not exhibit the strong surface cold pools that occur in association with high rainfall events. The ERA-Interim reanalysis, and to a lesser extent the ERA-40 reanalysis and the ECHAM5 model, does successfully exhibit some surface cooling in association with high rainfall events. In general, however, these differences suggest that, in both models and reanalyses, the transport of midtropospheric air with low moist static energy into the boundary layer via mesoscale downdrafts may be too weak.

In the tropics, rainfall heats and moistens the background atmosphere in such a way as to promote the propagation of coherent moving rainfall patterns. Models that are able to realistically simulate the short-time-scale impact of high rainfall events on the background atmosphere should also be more likely to simulate observed rainfall variability. Deep convection affects the water

vapor budget through vapor and condensation detrainment, precipitation evaporation, downdraft detrainment, induced subsidence from updrafts, and induced uplift from downdrafts. In a general circulation model, it is difficult to determine whether the relative contribution of each of these processes to the water vapor budget as a function of altitude is realistic. However, if the water vapor budget of a model is realistic, the effect of convection on the background humidity field on short time scales should be well simulated. The types of local diagnostic tests discussed here may be useful in guiding the development of more predictive convective parameterizations, both in terms of their rainfall forecasts on short time scales and their climate forecasts on longer time scales.

REFERENCES

Barnes, G. M., and M. Garstang, 1982: Subcloud layer energetics of precipitating convection. *Mon. Wea. Rev.,* **110,** 102–117.

Benedict, J., and D. A. Randall, 2007: Observed characteristics of the MJO relative to maximum rainfall. *J. Atmos. Sci.,* **64,** 2332–2354.

Dai, A., 2006: Precipitation characteristics in eighteen coupled climate models. *J. Climate,* **19,** 4605–4630.

Delworth, T. L., and Coauthors, 2006: GFDL's CM2 global coupled climate models. Part I: Formulation and simulation characteristics. *J. Climate,* **19,** 643–674.

DeMott, C., D. A. Randall, and M. Khairoutdinov, 2007: Convective precipitation variability as a tool for general circulation model analysis. *J. Climate,* **20,** 91–112.

Durre, I., R. S. Vose, and D. B. Wuertz, 2006: Overview of the integrated global radiosonde archive. *J. Climate,* **19,** 53–68.

Folkins, I., 2009: A one-dimensional cloud model with trimodal convective outflow. *J. Climate,* **22,** 6437–6455.

——, S. Fueglistaler, G. Lesins, and T. Mitovski, 2008: A low-level circulation in the tropics. *J. Atmos. Sci.,* **65,** 1019–1034.

Fovell, R. G., G. Mullendore, and S. H. Kim, 2006: Discrete propagation in numerically simulated nocturnal squall lines. *Mon. Wea. Rev.,* **134,** 3735–3752.

Houze, R. A., Jr., 2004: Mesoscale convective systems. *Rev. Geophys.,* **42,** RG4003, doi:10.1029/2004RG000150.

Huffman, G. J., and Coauthors, 2007: The TRMM Multisatellite Precipitation Analysis (TMPA): Quasi-global, multiyear, combined-sensor precipitation estimates at fine scales. *J. Hydrometeor.,* **8,** 38–55.

Johnson, R. H., 1976: The role of convective-scale precipitation downdrafts in cumulus and synoptic-scale interactions. *J. Atmos. Sci.,* **33,** 1890–1910.

——, P. E. Ciesielski, and K. A. Hart, 1996: Tropical inversions near the 0°C level. *J. Atmos. Sci.,* **53,** 1838–1855.

——, T. M. Rickenbach, S. A. Rutledge, P. E. Ciesielski, and W. H. Schubert, 1999: Trimodal characteristics of tropical convection. *J. Climate,* **12,** 2397–2418.

Khairoutdinov, M. F., S. K. Krueger, C.-H. Moeng, P. A. Bogenschutz, and D. A. Randall, 2009: Large-eddy simulation of maritime deep tropical convection. *J. Adv. Model. Earth Syst.,* **1,** 1–13.

Kummerow, C., W. Barnes, T. Kozu, J. Shiue, and J. Simpson, 1998: The Tropical Rainfall Measuring Mission (TRMM) sensor package. *J. Atmos. Oceanic Technol.,* **15,** 809–817.

Lohmann, U., and E. Roeckner, 1996: Design and performance of a new cloud microphysical scheme developed for the ECHAM general circulation model. *Climate Dyn.,* **12,** 557–572.

Maloney, E. D., and D. L. Hartmann, 1998: Frictional moisture convergence in a composite life cycle of the Madden–Julian oscillation. *J. Climate,* **11,** 2387–2403.

Mapes, B. E., 1993: Gregarious tropical convection. *J. Atmos. Sci.,* **50,** 2026–2037.

——, and R. A. Houze Jr., 1995: Diabatic divergence profiles in tropical mesoscale convective systems. *J. Atmos. Sci.,* **52,** 1807–1828.

——, and J. Lin, 2005: Doppler radar observations of mesoscale wind divergence in regions of tropical convection. *Mon. Wea. Rev.,* **133,** 1808–1824.

——, S. Tulich, J. Lin, and P. Zuidema, 2006: The mesoscale convection life cycle: Building block or prototype for large-scale tropical waves? *Dyn. Atmos. Oceans,* **42,** 3–29.

——, J. Bacmeister, M. Khairoutdinov, C. Hannay, and M. Zhao, 2009: Virtual field campaigns on deep tropical convection in climate models. *J. Climate,* **22,** 244–257.

McFarlane, N. A., J. F. Scinocca, M. Lazare, R. Harvey, D. Verseghy, and J. Li, 2005: The CCCma third generation atmospheric general circulation model. CCCma Internal Rep., 25 pp.

Nordeng, T. E., 1994: Extended versions of the convective parameterization scheme at ECMWF and their impact on the mean and transient activity of the model in the tropics. ECMWF Tech. Memo. 206, 41 pp.

Reed, R. J., and E. E. Recker, 1971: Structure and properties of synoptic-scale wave disturbances in the equatorial western Pacific. *J. Atmos. Sci.,* **28,** 1117–1133.

Roeckner, E., and Coauthors, 2003: The atmospheric general circulation model ECHAM5. Part 1: Model description. Max-Planck-Institute für Meteorologie Rep. 349, 127 pp.

Schumacher, C., and R. A. Houze Jr., 2003: Stratiform rain in the tropics as seen by the TRMM Precipitation Radar. *J. Climate,* **16,** 1739–1756.

——, P. E. Ciesielski, and M. H. Zhang, 2008: Tropical cloud heating profiles: Analysis from KWAJEX. *Mon. Wea. Rev.,* **136,** 4289–4300.

Scinocca, J. F., and N. A. McFarlane, 2004: The variability of modeled tropical precipitation. *J. Atmos. Sci.,* **61,** 1993–2015.

Sherwood, S. C., 1999: Convective precursors and predictability in the tropical western Pacific. *Mon. Wea. Rev.,* **127,** 2977–2991.

——, and R. Wahrlich, 1999: Observed evolution of tropical deep convective events and their environment. *Mon. Wea. Rev.,* **127,** 1777–1795.

Sobel, A. H., S. E. Yuter, C. S. Bretherton, and G. N. Kiladis, 2004: Large-scale meteorology and deep convection during TRMM KWAJEX. *Mon. Wea. Rev.,* **132,** 422–444.

Sun, Y., S. Solomon, A. Dai, and R. Portmann, 2006: How often does it rain? *J. Climate,* **19,** 916–934.

Takayabu, Y. N., K.-M. Lau, and C.-H. Sui, 1996: Observation of a quasi 2-day wave during TOGA COARE. *Mon. Wea. Rev.,* **124,** 1892–1913.

Tepper, M., 1950: A proposed mechanism of squall lines: The pressure jump line. *J. Meteor.,* **7,** 21–29.

Thompson, R. M., Jr., S. W. Payne, E. E. Recker, and R. J. Reed, 1979: Structure and properties of synoptic-scale wave disturbances in the intertropical convergence zone of the eastern Atlantic. *J. Atmos. Sci.,* **36,** 53–72.

Tiedtke, M., 1989: A comprehensive mass flux scheme for cumulus parameterization in large-scale models. *Mon. Wea. Rev.,* **117,** 1779–1800.

Tompkins, A. M., 2001: Organization of tropical convection in low vertical wind shears: the role of cold pools. *J. Atmos. Sci.,* **58,** 1650–1672.

——, 2002: A prognostic parameterization for the subgrid-scale variability of water vapor and clouds in large-scale models and its use to diagnose cloud cover. *J. Atmos. Sci.,* **59,** 1917–1942.

Uppala, S. M., and Coauthors, 2005: The ERA-40 Re-Analysis. *Quart. J. Roy. Meteor. Soc.,* **131,** 2961–3012.

von Salzen, K., N. A. McFarlane, and M. Lazare, 2005: The role of shallow convection in the water and energy cycles of the atmosphere. *Climate Dyn.,* **25,** 671–688.

Zhang, G. J., and N. A. McFarlane, 1995: Sensitivity of climate simulations to the parameterization of cumulus convection in the CCC-GCM. *Atmos.–Ocean,* **3,** 407–446.

Zipser, E. J., 1969: The role of organized unsaturated convective downdrafts in the structure and rapid decay of an equatorial disturbance. *J. Appl. Meteor.,* **8,** 799–814.

——, 1977: Mesoscale and convective-scale downdrafts as distinct components of a squall-line structure. *Mon. Wea. Rev.,* **105,** 1568–1589.

Zuidema, P., 1998: The 600–800-mb minimum in tropical cloudiness observed during TOGA COARE. *J. Atmos. Sci.,* **55,** 2220–2228.